CRYSTAL GROWTH & DESIGN

pubs.acs.org/crystal

Article

Cooperativity of Halogen- and Chalcogen-Bonding Interactions in the Self-Assembly of 4-Iodoethynyl- and 4,7-Bis(iodoethynyl)benzo-2,1,3-chalcogenadiazoles: Crystal Structures, Hirshfeld Surface Analyses, and Crystal Lattice Energy Calculations

Jan Alfuth, Beata Zadykowicz, Barbara Wicher, Katarzyna Kazimierczuk, Tadeusz Połoński, and Teresa Olszewska*

Cite This: *Cryst. Growth Des.* 2022, 22, 1299–1311

Read Online

ACCESS | Metrics & More | Article Recommendations | Supporting Information

ABSTRACT: Several new 4-iodoethynyl- and 4,7-bis(iodoethynyl)benzo-2,1,3-chalcogenadiazoles were prepared, and a comprehensive analysis of the most prominent secondary bonding interactions responsible for the crystal self-assembly was performed using X-ray diffraction. The presence of both the iodoethynyl and chalcogenadiazole moieties allows an evaluation of the preference of these molecules to aggregate through either chalcogen- or halogen-bonding interactions in the solid state. The crystal structures of the compounds revealed that their solid-state arrangements are influenced by the nature of the chalcogen atom: for the crystals of the thiadiazoles studied, the ≡C−I···N halogen bonds were preferred, whereas in the corresponding 2,1,3-selenadiazole derivatives, the self-complementary $[Se\cdots N]_2$ supramolecular synthons together with the ≡C−I···N halogen-bonding interactions determined the molecular self-assembly. Furthermore, in the case of the bis(iodoethynyl) derivative the crystal structure was additionally influenced by the ≡C−I···π(ethynyl) halogen bond. Hirshfeld surface and 2D fingerprint plot analyses were used to demonstrate the intermolecular interactions and intercontact distributions. Also, the total lattice energies were calculated using the CRYSTAL09 and CrystalExplorer programs. They both indicated intermolecular $\pi\cdots\pi$ interactions as the forces of substantial contribution to the total lattice energies.

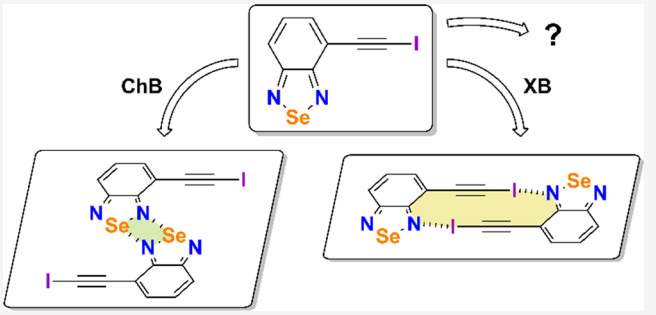

INTRODUCTION

A rational design of functional materials is not possible without a deep understanding of forces responsible for the aggregation of molecules in the solid state.[1,2] Therefore, different classes of noncovalent intermolecular interactions, ranging from very weak contacts, such as van der Waals interactions, through middle-strength $\pi\cdots\pi$ interactions, to strong forces, such as hydrogen bonds, are currently receiving a great deal of attention.[3−5] Among them, σ-hole bonds[6] are of special interest, as they are relatively new and have not yet been fully explored. They are schematically represented as X−E···Y, where the positive electrostatic potential occurring in a molecular entity X−E interacts with a nucleophilic region Y in another or the same molecule.[7,8] When the central polarizable atom E represents elements of groups 15−17 of the periodic table, the interactions are referred to as pnictogen (PnB),[9,10] chalcogen (ChB),[11,12] and halogen bonds (XB),[13−15] respectively. Their features and properties are explained in terms of electrostatics, polarization, and dispersion.[16] Without a doubt, halogen bonds have been the most extensively studied, and their importance has been evaluated in materials science, supramolecular chemistry, and biological systems.[1,17−19] Chalcogen bonding, although defined by IUPAC only in 2019,[20] has already found many applications: namely, in crystal engineering,[21] materials chemistry,[22,23] optoelectronics,[24] medicinal chemistry,[25] molecular recognition,[26] and organocatalysis.[27−30] One of the attributes of XB and ChB is their high directionality and strength tunability, which are essential in programing new noncovalent three-dimensional architectures. The main difference between XB and ChB results from the valence electronic structure. On a neutral halogen atom there is at most one σ-hole,[13,31] whereas a chalcogen atom is able to form two σ-hole interactions at the extension of the covalent bonds in which it is involved.[32,33]

Received: October 31, 2021
Revised: January 2, 2022
Published: January 18, 2022

https://doi.org/10.1021/acs.cgd.1c01266
Cryst. Growth Des. 2022, 22, 1299−1311

Representative examples of ChBs are the structures of 1,2,5-telluradiazole[34,35] and phenanthro[9,10-*c*][1,2,5]-telluradiazole,[36] whose molecules organize through cyclic four-membered $[Te\cdots N]_2$ supramolecular synthons into ribbons in the solid state. In this arrangement, each Te atom forms two bifurcated chalcogen bonds. Other examples include cocrystals of 3,4-dicyano-1,2,5-chalcogenadiazoles with substituted pyridine *N*-oxides[37] and other Lewis bases.[38] However, double-chalcogen-bond systems are not always observed. This is mainly due to the proximity of both σ-holes, which prevents the coordination of two sterically crowded nucleophiles.[39] The formation of a single X−E···Y interaction during the self-assembly process is more common for lighter chalcogen atoms such as sulfur. A detailed classification of molecular motifs based on chalcogen-bonding interactions is described in the work published by Bonifazi and co-workers.[40]

Among the elements recognized as donors of chalcogen bonds, namely sulfur, selenium, and tellurium atoms, the last element forms the strongest ChBs.[41] Nonetheless, compounds containing sulfur and selenium atoms have been the most frequently studied. The main reason for this is that sulfur can participate in all kinds of different interactions: for example, as an acceptor of hydrogen or halogen bonds. Second, sulfur- and selenium-containing molecules are present in living organisms and are of interest for pharmaceutical applications. In turn, tellurium compounds are usually prone to decomposition due to their air and moisture sensitivity. Moreover, their synthesis is often much more challenging.

Most of the XB and ChB molecular motifs reproduced by self-aggregating molecules with high recognition fidelity have been provided by crystal engineering. Molecules in which XB or ChB donors and acceptors are incorporated in the rigid skeleton close to each other, such as in chalcogenazolo[5,4-β]pyridines[42] or benzo-2,1,3-chalcogenadiazoles and their derivatives,[43] constitute a highly desirable model for this kind of study. In the absence of any additional functional group, the heterocycle moieties of benzo-2,1,3-chalcogenadiazoles assemble through single- or double-chalcogen-bonding E···N interactions to form dimeric or polymeric structures, and their geometric arrangements can be modulated by the size and position of the substituents.

Continuing our interest in the construction of supramolecular assemblies with the use of ChBs,[44,45] we decided to exploit a group of benzo-2,1,3-chalcogenadiazoles bearing one or two iodoethynyl substituents at the 4- or 4,7-positions (Scheme 1). The self-assembly process of these compounds can be driven by the formation of halogen or chalcogen bonds or both of these interactions.

It is worth mentioning that the simultaneous use of XB and ChB interactions in supramolecular assemblies has been marginally investigated.[45,46] However, during the review procedure of this paper, a closely related paper dealing with the competition between different σ-hole interactions in the crystals of 4,7-dihalogeno- and 4,7-bis(halogenoethynyl)benzo-2,1,3-chalcogenadiazoles was published by Aakeröy and co-workers.[47] The iodoethynyl moiety in our model compounds was chosen as a substituent because the iodine atom attached to sp-hybridized carbon tends to form strong halogen bonds.[48] Moreover, due to the location of the substituent close to the nitrogen atom of the chalcogenadiazole ring, the molecules of the title compounds are able to form a self-complementary XB interaction.

Scheme 1. Molecular Structures of the Designed Iodoethynyl-Substituted Benzo-2,1,3-chalcogenadiazoles

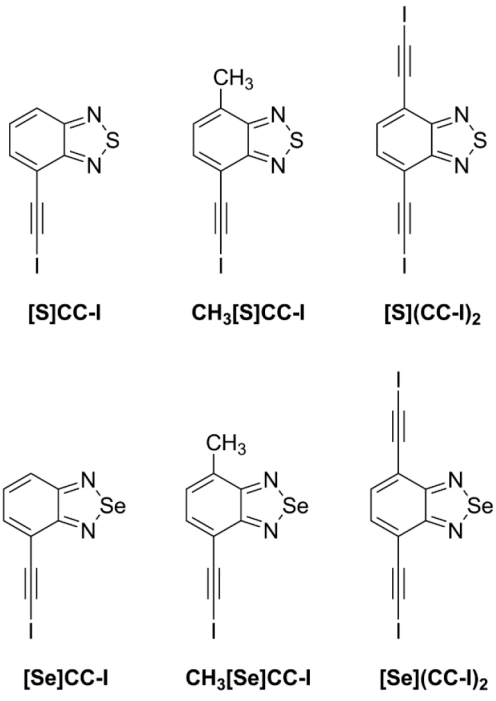

The molecules of the designed compounds contain one S or Se atom acting as the ChB donor, one or two iodine atoms as the XB donor, and two nitrogen atoms as acceptors of either ChB or XB (Scheme 2). Thus, upon crystallization, these compounds could aggregate through one of the arrangements shown in Scheme 3.

Scheme 2. Depiction of a Molecule of the Designed Benzo-2,1,3-chalcogenadiazole (E = S, Se; R = H, CH_3, −C≡C−I) with Highlighted Halogen (Purple Arrow) and Chalcogen Bond Donors (Orange Arrows) and Acceptors (Blue Arrows)

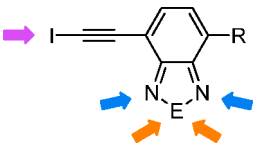

The chalcogenadiazoles substituted with one iodoethynyl moiety and in the absence of ChB interactions are expected to form the infinite-chain polymers **I** with the use of XB interactions or dimers **II** through self-complementary XB bonding. However, the analogous chalcogenadiazoles able to form strong ChB interactions could self-assemble into chain **III** or double-chain **IV** polymers held together by both XBs and self-complementary $[E\cdots N]_2$ interactions. On the other hand, in the case of the chalcogenadiazole molecule bearing two iodoethynyl units in the absence of the ChB it is expected to create the chain polymer **V** through self-complementary XB bonds or the more complex 2D structure **VI** held together by XB interactions, whereas cooperation of the XB with ChB interactions would result in the chain structure **VII**, closely related to that of **III**, composed of chalcogenazole dimers connected by XB interactions.

https://doi.org/10.1021/acs.cgd.1c01266
Cryst. Growth Des. 2022, 22, 1299−1311

Scheme 3. Proposed Supramolecular Motifs for the Studied Compounds (E = S, Se; R = H, CH_3)

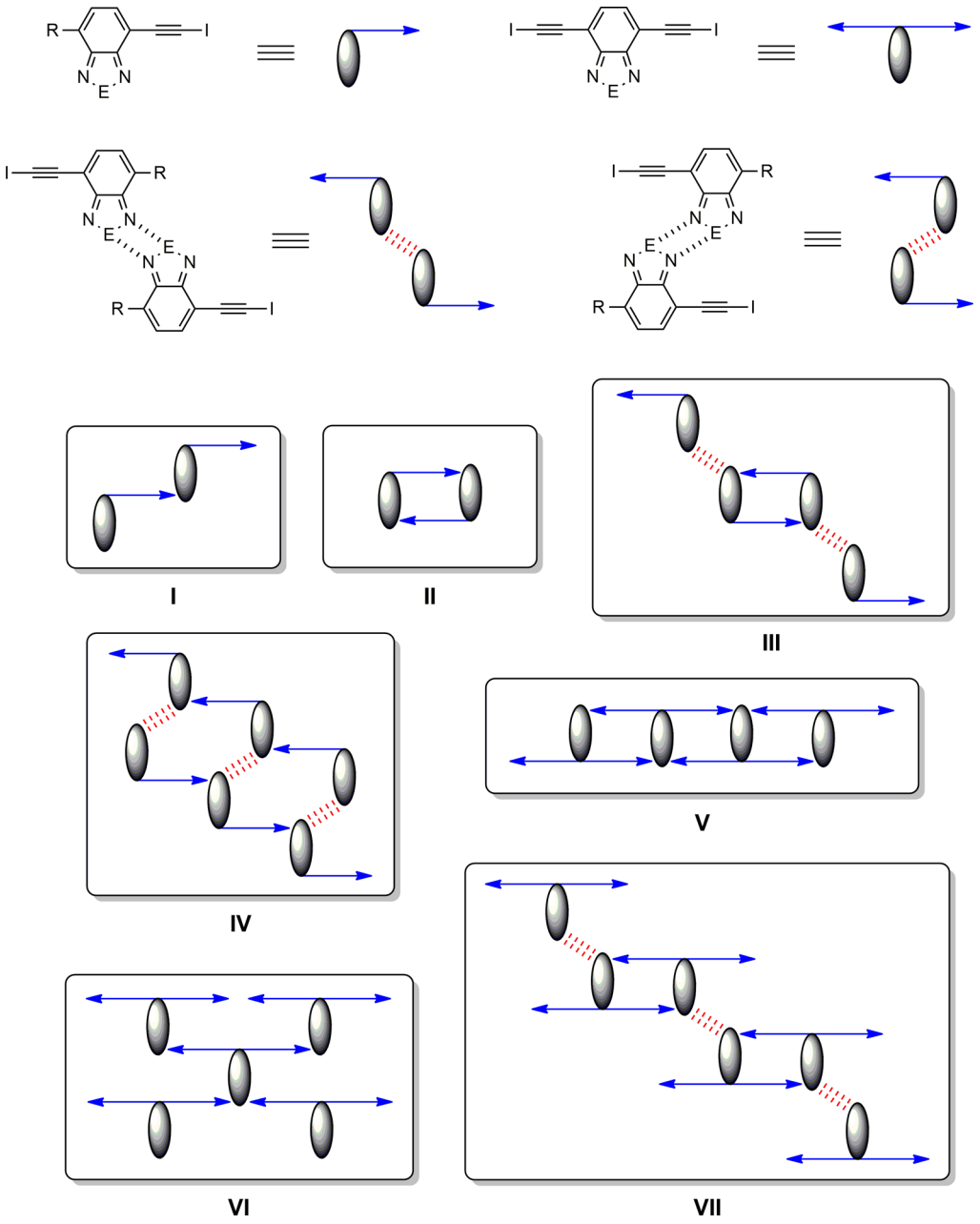

In order to explore the effect of a simultaneous contribution of XB and ChB interactions on the supramolecular structures of the title benzo-2,1,3-chalcogenadiazoles, we synthesized the compounds shown in Scheme 1 and determined their crystal structures. In the next step, we used Hirshfeld surface and 2D fingerprint plot analyses[49,50] to demonstrate the intermolecular interactions and intercontact distributions. Finally, we calculated the total lattice energies to assess the contributions from individual intermolecular forces to the stability of the crystal lattices.

EXPERIMENTAL METHODS

All of the benzo-2,1,3-chalcogenadiazoles derivatives were synthesized by simple several-step reactions, starting from commercially available *o*-phenylenediamine for **[S]CC-I**, **[S](CC-I)$_2$**, **[Se]CC-I**, and **[Se](CC-I)$_2$** and 3-methyl-*o*-phenylenediamine for **CH$_3$[S]CC-I** and **CH$_3$[Se]CC-I**. For five of the compounds, their crystals suitable for X-ray analysis were obtained by a slow evaporation method. The detailed synthesis, crystallization procedures, and characterization data are summarized in the Supporting Information.

X-ray Diffraction (XRD). Reflection intensities were measured at 130 K using an Oxford Diffraction SuperNova diffractometer equipped with high-flux microfocus Nova CuKα radiation. The data were processed with CrysAlis PRO software.[51] Absorption corrections were made using the implemented methods: analytical[52] or Gaussian in case of **[S](CC-I)$_2$**. The structures were solved using a dual-space algorithm with SHELXT 2018/2.[53] Using Olex2 1.3[54] the structures were refined by full-matrix least squares based on F^2 with SHELXL 2018/3.[53] All of the non-H atoms were refined anisotropically. The C-bound H atoms were constrained to their calculated positions and refined as riding on their pivot atoms with U_{iso}(H) = 1.2U_{eq}(C) or 1.5U_{eq}(methyl C). The ORTEP representations of the asymmetric units of the presented crystals are shown in Figure S1 in the Supporting Information.

Powder X-ray Diffraction (PXRD). The XRD patterns of the samples were recorded on a Bruker AXS D2 Phaser diffractometer

https://doi.org/10.1021/acs.cgd.1c01266
Cryst. Growth Des. 2022, 22, 1299−1311

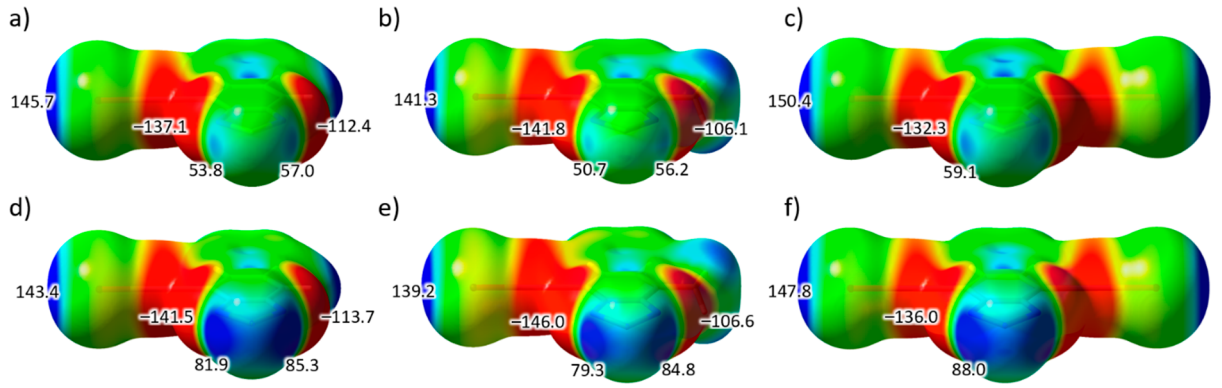

Figure 1. Molecular electrostatic potential mapped on 0.001 au molecular isosurfaces of the electron density: (a) [**S**]**CC-I**; (b) **CH$_3$**[**S**]**CC-I**; (c) [**S**](**CC-I**)$_2$; (d) [**Se**]**CC-I**; (e) **CH$_3$**[**Se**]**CC-I**; (f) [**Se**](**CC-I**)$_2$. The opaque surfaces are presented with a colored scale, which corresponds to values ranging from −0.025 (red) to +0.025 au (blue). The most positive ($V_{S,max}$) and negative ($V_{S,min}$) electrostatic potential values (in kJ mol^{-1}) are indicated.

with Cu Kα radiation (λ = 1.5418 Å). The operating voltage and current were maintained at 30 kV and 10 mA, respectively. The samples were scanned from 5 to 45° 2θ. The scans were made with a step size of 0.02°, a counting rate of 2 s/step, and spinning of the sample. The acquired data were analyzed using SigmaPlot for Windows 11.0, Build 11.0.0.77 (Systat Software, Inc., 2008) and are shown in Figure S2 in the Supporting Information.

Theoretical Calculations. The evaluation of the molecular electrostatic potential was conducted using the Gaussian09 package.[55] The geometry optimizations of isolated molecules were carried out at the DFT(B3LYP)/6-31G**[56−60] (and DFT(B3LYP)/3-21G* for the iodine atom[61]) level of theory. The B3LYP functional is known to produce reliable results for the thermodynamic data and has been proven to provide accurate qualitative results for the molecular electrostatic potential of similar molecules.[62−64] Molecular electrostatic potential (MEP) maps were visualized with GaussView 5.0.8,[65] and then the maximum and minimum values of the electrostatic potential ($V_{S,max}$ and $V_{S,max}$) on individual atoms were calculated.

The geometry of all the crystal structures was optimized at the DFT(B3LYP)/6-31G**[56−60] (and DFT(B3LYP)/3-21G* for the iodine atom[61]) level of theory in the Crystal program (CRYSTAL09 version)[66] prior to further computational analyses. During the optimization procedure the cell parameters were kept fixed while the atom positions were varied. Crystal cohesive energies for the studied crystal systems were calculated at the same level of theory. The results were corrected for dispersion[67−69] and the basis set superposition error (BSSE).[70] Ghost atoms used for the BSSE estimation were selected up to a distance of 5 Å from the considered molecule in the crystal lattice.

The Hirshfeld surfaces and fingerprint plots were generated using the CrystalExplorer17 program.[71] The intermolecular interaction energies were also determined using the Hartree−Fock method[72] and the 3-21G basis set[61,73] implemented in the CrystalExplorer17 program. The atomic coordinates used in the calculations were obtained from the crystallographic data.

RESULTS AND DISCUSSION

Electrostatic Potential Maps. In order to acquire a deeper insight into the regions susceptible to potential interaction, molecular electrostatic potential (MEP) calculations were performed for the six investigated compounds (Figure 1).

The 3D contour maps of the MEP show the expected anisotropic distribution of electron density around the iodine atom with an electron-deficient region at the tip of the C−I bond, a so-called σ-hole. The magnitude of the local maximum of the electrostatic potential ($V_{S,max}$) at the iodine atom is slightly lower for **CH$_3$**[**S**]**CC-I** and **CH$_3$**[**Se**]**CC-I** than for the remaining chalcogenadiazoles. The MEP surfaces additionally reveal the presence of two regions with positive electrostatic potential at the chalcogen atoms. Both σ-holes are more pronounced on selenium atoms than on sulfur atoms, and the local MEP values for Se are approximately 30 kJ mol^{-1} higher (about one and a half times higher) than for S. Moreover, the positive charge is not concentrated symmetrically on both sides of the chalcogen atom for derivatives bearing one (iodoethynyl) or two (iodoethynyl and methyl) different substituents attached to the benzene ring. The results are in line with previously published data indicating that the $V_{S,max}$ values on the chalcogen atom in chalcogenadiazoles can be tuned by the electronegativity of the substituent and the substitution pattern of chalcogenadiazoles.[16,74] For the compounds studied, the higher energy value of the electrophilic region is located opposite the −C≡C−I substituent. This suggests that the σ-hole is slightly more prone to interact with a nucleophile. On the other hand, other energy components not included in the MEP may also play a pivotal role.

Crystal Structure Descriptions. 4-Iodoethynylbenzo-2,1,3-thiadiazole ([**S**]**CC-I**) crystallizes in the monoclinic space group $P2_1/m$ (Z' = 0.5), with half of the molecule in an asymmetric unit located on a mirror plane. The [**S**]**CC-I** molecules interact through ≡C−I···N XBs, forming infinite chains (motif **I**, Figure 2a). The distance between the I and N atoms is 2.907(6) Å, which is 17% shorter than the sum of their van der Waals radii ($\delta_{\%}$ = 83%), while the valence angle of this bond has an advantageous value of 178.5(2)° (Table 1). Through weak C$_{Ar}$−H···I hydrogen bonds (Table 1) the chains aggregate into (010) polar sheets where the −C≡C−I substituents are oriented in the same direction. However, the symmetry center relates the adjacent layers, which leads to the cancellation of the bulk polarity (Figure 2b). The 3D structure is stabilized by $\pi\cdots\pi$ stacking interactions between the benzene rings of the [**S**]**CC-I** molecules (Table 2 and Figure S3 in the Supporting Information).

An additional iodoethynyl substituent at the 7-position causes a complete change of the crystal structure of [**S**](**CC-I**)$_2$. Its crystals belong to the monoclinic crystal system, space group $P2_1/c$ (Z' = 1). The molecules arrange themselves in centrosymmetric dimers stabilized by XBs (motif **II**), forming $R_2^2(12)$ rings (Figure 3a). The N···I length is 3.064(8) Å ($\delta_{\%}$ = 87%), and the valence angle is 165.9(2)°. The geometric parameters of this interaction suggest that it should have

https://doi.org/10.1021/acs.cgd.1c01266
Cryst. Growth Des. 2022, 22, 1299−1311

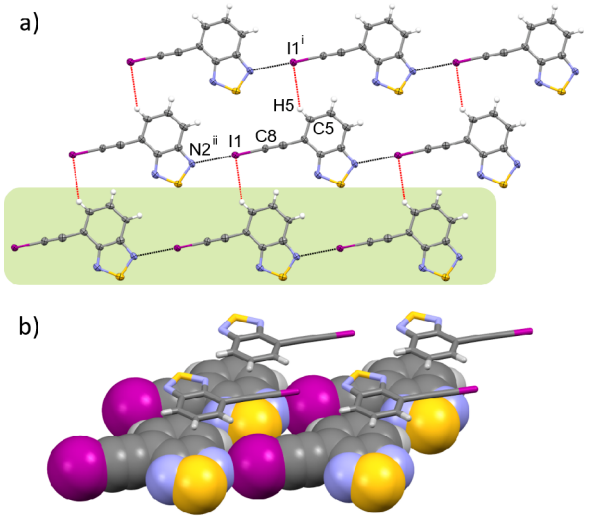

Figure 2. Crystal structure of [S]CC-I: (a) polar (010) sheet formed via weak hydrogen bonds (red dotted lines); the single chain is marked with a green rectangle and is stabilized with halogen bonds (black dotted lines); (b) fragment of the two antiparallel layers. Symmetry codes: (i) −1 + *x*, *y*, *z*; (ii) 1 + *x*, *y*, 1 + *z*.

slightly lower energy in comparison to that present in [S]CC-I. In the crystal lattice of [S](CC-I)$_2$ individual dimers are further connected with each other through ≡C−I···π(ethynyl) XBs, creating zigzag structures (Figure 3b and Table 3). This structure has been also reported by Aakeröy and co-workers.[47]

Surprisingly, the crystal structure of CH$_3$[S]CC-I contains none of the predicted supramolecular motifs. Still, as expected, the crystal structure is governed by XB interactions. The ≡C−I···N XBs link CH$_3$[S]CC-I molecules in helices extended along [010] with iodoethynyl substituents directed to the interior (Figure 4a). Despite the molecules being twisted in the helices, geometrical parameters of the XB interactions have advantageous values. The I···N distance is ca. 0.5 Å shorter than the sum of van der Waals radii of I and N atoms, and the ≡C−I···N angle has a value of 173.7(1)° (Table 1). The adjacent helices interact through two kinds of stacking interactions. In the first, the benzene ring is placed above the thiadiazole ring (Figure 4b); in the second, two benzene rings overlap. In such a way, a 3D structure is formed (Figure 4c and Table 2).

Table 2. Parameters of Stacking Interactions[a]

compound	Cg^b···Cg^b	Cg^b···Cg^c	Cg^{all}···Cg^{all}	Cg^b···pln	slippage
[S]CC-I	3.545			3.278	1.350
CH$_3$[S]CC-I		3.628		3.393	1.284
	3.656			3.430	1.265
[Se]CC-I		3.726		3.456	1.392
CH$_3$[Se]CC-I					
molecule A			3.472	3.341[b]	0.945
molecule B			3.549	3.428[b]	0.941

[a]Cg^b and Cg^c are centroids calculated for benzene and chalcogenadiazole rings, respectively, and Cg^{all} and pln is the centroid and the plane calculated for both rings, respectively. The slippage represents the relative shift of the centroids in the stacking pair. It is calculated on the basis of the Pythagorean theorem. All of the values are expressed in Å. [b]Cg^{all}···pln values instead of Cg^b···pln are reported.

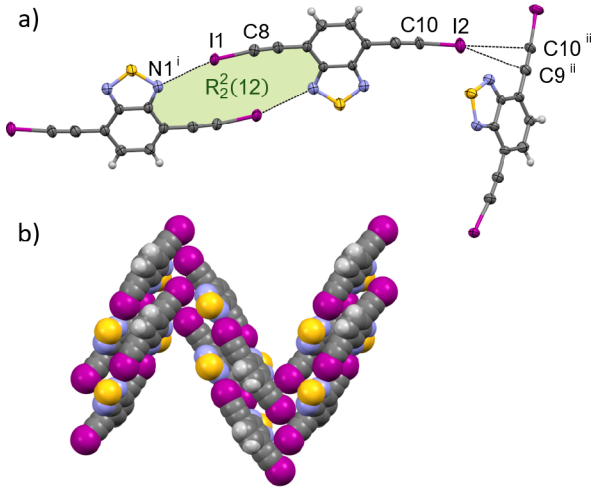

Figure 3. Crystal structure of [S](CC-I)$_2$: (a) representation of the dimer and the ≡C−I···π(ethynyl) interaction (along with labels of the atoms involved in secondary interactions); (b) fragment of the zigzag structures. Symmetry codes: (i) 1 − *x*, −*y*, 1 − *z*; (ii) −*x*, 0.5 + *y*, 1.5 − *z*.

Table 1. Bond Lengths, Dihedral Angles, and $\delta_{\%}$ Parameters of selected X−E···Y Intermolecular Interactions[a]

compound	X−E···Y	d_{X-E} (Å)	$d_{E\cdots Y}$ (Å)	$\theta_{X-E\cdots Y}$ (deg)	$\delta_{\%}$ (%)	symmetry code (i)
[S]CC-I	C8−I1···N2^i	2.007(6)	2.907(6)	178.5(2)	82	1 + *x*, *y*, 1 + *z*
	C5−H5···I1^i	0.95	3.109(6)	143		−1 + *x*, *y*, *z*
[S](CC-I)$_2$	C8−I1···N2^i	2.002(8)	3.064(8)	165.9(2)	87	1 − *x*, − *y*, 1 − *z*
CH$_3$[S]CC-I	C8−I1···N1^i	2.013(3)	3.025(3)	173.7(1)	86	1.5 − *x*, −0.5 + *y*, 1.5 − *z*
[Se]CC-I	C8−I1···N2^i	2.021(4)	2.935(3)	171.6(1)	84	−1 + *x*, 1 + *y*, *z*
	N2−Se1···N1^i	1.792(3)	2.880(3)	163.4(1)	84	1 − *x*, 1 − *y*, 1 − *z*
	C4−H4···I1^i	0.95	3.352(6)	158		2 − *x*, 1 − *y*, 2 − *z*
CH$_3$[Se]CC-I	C8A−I1A···N1B^i	2.012(4)	2.985(4)	167.6(1)	85	*x*, *y*, 1 + *z*
	C8B−I1B···N1A^i	2.008(4)	3.013(4)	165.5(1)	86	*x*, *y*, −1 + *z*
	N1A−Se1A···N2B^i	1.789(4)	2.869(4)	165.4(1)	83	
	N1B−Se1B···N2A^i	1.792(4)	2.867(4)	165.2(1)	83	
	C4A−H4A···I1B^i	0.95	3.252(6)	149		*x*, −1 + *y*, 1 + *z*
	C4B−H4B···I1A^i	0.95	3.223(6)	152		*x*, 1 + *y*, −1 + *z*

[a]The parameter $\delta_{\%}$ corresponds to the ratio of the length of secondary interaction and the sum of van der Waals radii of two interacting atoms according to the following equation: $\delta_{\%} = \frac{d_{E\cdots Y}}{r_{vdW_E} + r_{vdW_Y}} \times 100\%$. When E is an H atom with a fixed distance C−H (X−E), the $\delta_{\%}$ values are not given.

https://doi.org/10.1021/acs.cgd.1c01266
Cryst. Growth Des. 2022, 22, 1299−1311

Table 3. Bond Lengths, Distances, and Dihedral Angles of Selected C−E···π(ethynyl) Intermolecular Interactions[a]

compound	C−E···π	d_{C-E} (Å)	$d_{E\cdots\pi}$ (Å)	$\theta_{C-E\cdots\pi}$ (deg)	symmetry code (i)
[S](CC-I)$_2$	C10−I2···π^i	2.003(8)	3.409	164.7	$-x$, 0.5 + y, 1.5 − z
[Se]CC-I	C5−H5···π^i	0.95	3.127	145	2 − x, 1 − y, 2 − z
CH$_3$[Se]CC-I	C5A−H5A···π^i	0.95	2.911	153	x, −1 + y, 1 + z
	C5B−H5B···π^i	0.95	2.900	155	x, 1 + y, −1 + z

[a]π(ethynyl) is represented as a centroid calculated for the C≡C bond.

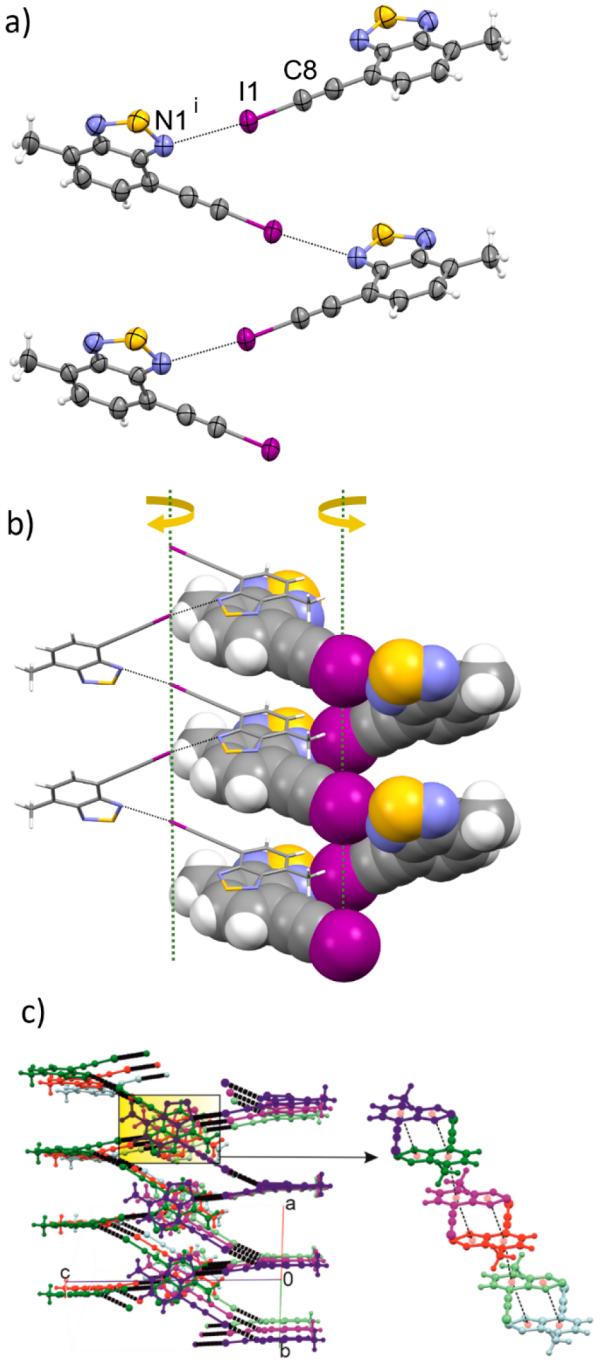

Figure 4. Crystal structure of CH$_3$[S]CC-I: (a) single helix stabilized by halogen bonds; (b) representation of two interpenetrating helices; (c) 3D structure formed through stacking interactions. Different helices are marked with different colors. Symmetry code: (i) 1.5 −x, −0.5 + y, 1.5 − z.

As expected, replacing the sulfur atom with selenium enhances the formation of ChB, and the [Se···N]$_2$ synthon is formed in the crystal structure of [Se]CC-I. Z-shaped dimers (motif IV) are connected by XBs into [1−10] chains (Figure 5a). These 1D motifs have corrugated edges, and adjacent

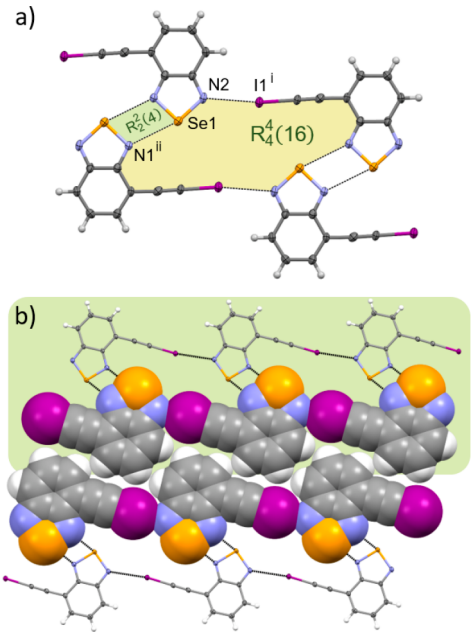

Figure 5. Crystal structure of [Se]CC-I: (a) representation of the tetramer (with labels of the atoms involved in secondary interactions); (b) (11−1) layer of molecules, where one chain is marked with a green rectangle and molecules at the contact surface between the chains are shown with a space-filling representation. Halogen and chalcogen interactions are shown as dotted black lines. Symmetry codes: (i) 1 + x, −1 + y, z; (ii) 1 − x, 1 − y, 1 − z.

chains are connected by following the groove and ridges principle. The benzene ring of one chain enters the groove of the other, thus forming a (11−1) layer. This arrangement is supported by weak C−H···I and C$_{Ar}$−H···π(ethynyl) interactions (Figure 5b and Tables 1 and 3). π-stacking interactions between the benzene and selenadiazole rings from the neighboring sheets (Table 2) stabilize the 3D structure. Unlike in other crystals, the stacking dimers are not centrosymmetric, and adjacent layers are only shifted, leaving the exact orientation of the [Se]CC-I molecules (Figure S4 in the Supporting Information). The crystal structure can also be viewed as infinite chains (as in [S]CC-I), arranged in an antiparallel fashion and connected by the [Se···N]$_2$ synthons (Figure 5b).

The CH$_3$[Se]CC-I crystal also belongs to space group $P\bar{1}$ but has two molecules, A and B, in the asymmetric unit (Z' = 2). These molecules, through the ChBs, form the [Se···N]$_2$ synthons. However, in this case, this motif is noncentrosym-

https://doi.org/10.1021/acs.cgd.1c01266
Cryst. Growth Des. 2022, 22, 1299−1311

metric (Figure 6a). The extension of the dimer to the [001] chain is completed through ≡C−I···N bonds, leading to motif

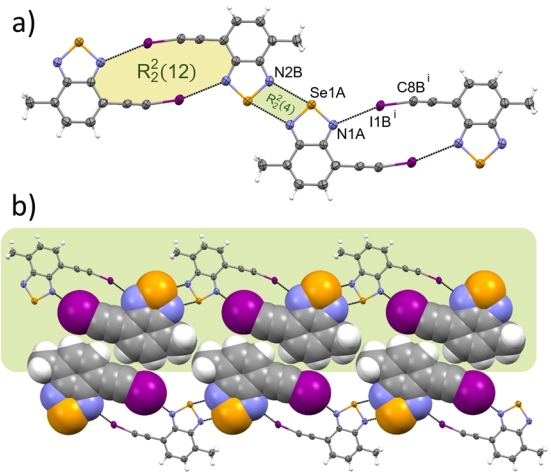

Figure 6. Crystal structure of CH_3[Se]CC-I: (a) representation of the chain (with labels of the atoms involved in secondary interactions); (b) fragment of the layer of molecules, where one chain is marked with a green rectangle and the molecules at the contact edges between the chains are shown with a space-filling representation. Halogen and chalcogen interactions are shown as dotted black lines. Symmetry code: (i) *x*, *y*, 1 + *z*.

III. Rebuilding the chain facilitates the formation of larger grooves at the edges in comparison to those in [**Se**]**CC-I**, which in turn allows entry of the methyl group alongside the benzene ring (Figure 6b). Still, weak C−H···I and C_{Ar}−H···π(ethynyl) interactions are observed to support the creation of (100) sheets (Tables 1 and 3). In this case, adjacent layers are not only shifted as in [**Se**]**CC-I** but also inverted through the symmetry center. This allows the overlapping of whole molecules (Table 2 and Figure S5 in the Supporting Information).

The main difference in the crystal structures of [**Se**]**CC-I** and CH_3[**Se**]**CC-I** arises from the use of different σ-holes located on the selenium atoms. The molecules of the methyl derivative form $[Se\cdots N]_2$ synthons using the electrophilic region, with a slightly higher positive electrostatic potential being found opposite the ethynyl moiety (Figure 1, motif **III**), whereas [**Se**]**CC-I** molecules utilize a σ-hole with a lower value of $V_{S,max}$ on the same side as the iodoethynyl group (Figure 1, motif **IV**).

Despite many attempts to crystallize [**Se**](**CC-I**)$_2$, we were unable to obtain good-quality crystals suitable for X-ray diffraction.

Table 4 provides crystal data for the studied compounds.

Hirshfeld Surface Analysis and Fingerprint Plots. Intermolecular interactions influencing the packing of the molecules in crystals were inspected using a Hirshfeld surface (HS) analysis.[49,50] The molecular HS for each chalcogenadiazole studied generated from the CrystalExplorer17 program are presented in Figure 7. We used normalized contact distances (d_{norm}) parameters[50] and 2D fingerprint plots to identify noncovalent interactions. In this concept, the color scale reflects intermolecular distances. Spots on the Hirshfeld surface correspond to distances between two considered atoms: bright red denotes shorter than, white equal to, and blue longer than the sum of their van der Waals (vdW) radii.

In [**S**]**CC-I** and CH_3[**S**]**CC-I**, one N···I type XB interaction (involving N2···I1 for [**S**]**CC-I** and N1···I1 for CH_3[**S**]**CC-I**) displayed intense red areas. The strengths of these interactions, also obtained from the CrystalExplorer program, are −17.7 and

Table 4. Crystal Data and Refinement Details

	[S]CC-I	[S](CC-I)$_2$	[Se]CC-I	CH_3[S]CC-I	CH_3[Se]CC-I
CCDC no.	2101347	2101344	2101348	2101346	2101345
empirical formula	$C_8H_3IN_2S$	$C_{10}H_2I_2N_2S$	$C_8H_3IN_2Se$	$C_9H_5IN_2S$	$C_9H_5IN_2Se$
formula wt	286.08	436.00	332.98	300.11	347.01
cryst syst	monoclinic	monoclinic	triclinic	monoclinic	triclinic
space group	$P2_1/m$	$P2_1/c$	$P\bar{1}$	$C2/c$	$P\bar{1}$
temp (K)	130	130	130	130	130
a, *b*, *c* (Å)	7.1869(5), 6.5569(4), 9.1958(5)	7.7624(3), 7.8688(3), 18.3856(7)	4.0859(2), 10.4759(5), 11.1405(6)	14.1112(3), 7.3656(2), 18.8739(4)	6.8522(1), 10.2290(2), 14.4493(3)
α, β, γ (deg)	90, 99.757(6), 90	90, 99.064(3), 90	64.627(5), 82.096(4), 80.144(4)	90, 94.167(2), 90	73.204(2), 82.360(2), 88.572(2)
V (Å^3)	427.07(4)	1108.98(8)	423.39(4)	1956.53(9)	960.86(4)
Z	2	4	2	8	4
calcd density (g/cm^3)	2.225	2.611	2.612	2.038	2.399
μ (mm^{-1})	31.25	46.03	34.14	27.33	30.12
no. of rflns collected	5984	8345	5700	17001	42888
no. of rflns obsd ($I > 2\sigma(I)$)	934	1896	1659	1889	3724
R_{int}	0.090	0.075	0.028	0.075	0.104
no. of data/params	948/73	2181/137	1671/109	1999/119	3925/237
S	1.096	1.041	1.133	1.069	1.058
final *R* indices ($F^2 > 2\sigma(F^2)$)	R_1 = 0.041	R_1 = 0.049	R_1 = 0.024	R_1 = 0.029	R_1 = 0.039
	wR_2 = 0.106	wR_2 = 0.127	wR_2 = 0.066	wR_2 = 0.075	wR_2 = 0.108
R indices (all data)	R_1 = 0.042	R_1 = 0.055	R_1 = 0.024	R_1 = 0.030	R_1 = 0.041
	wR_2 = 0.106	wR_2 = 0.136	wR_2 = 0.066	wR_2 = 0.077	wR_2 = 0.111
largest peak, hole (e Å^{-3})	1.07, −1.05	1.30, −1.34	0.72, −0.61	0.75, −0.95	1.19, −1.32

https://doi.org/10.1021/acs.cgd.1c01266
Cryst. Growth Des. 2022, 22, 1299−1311

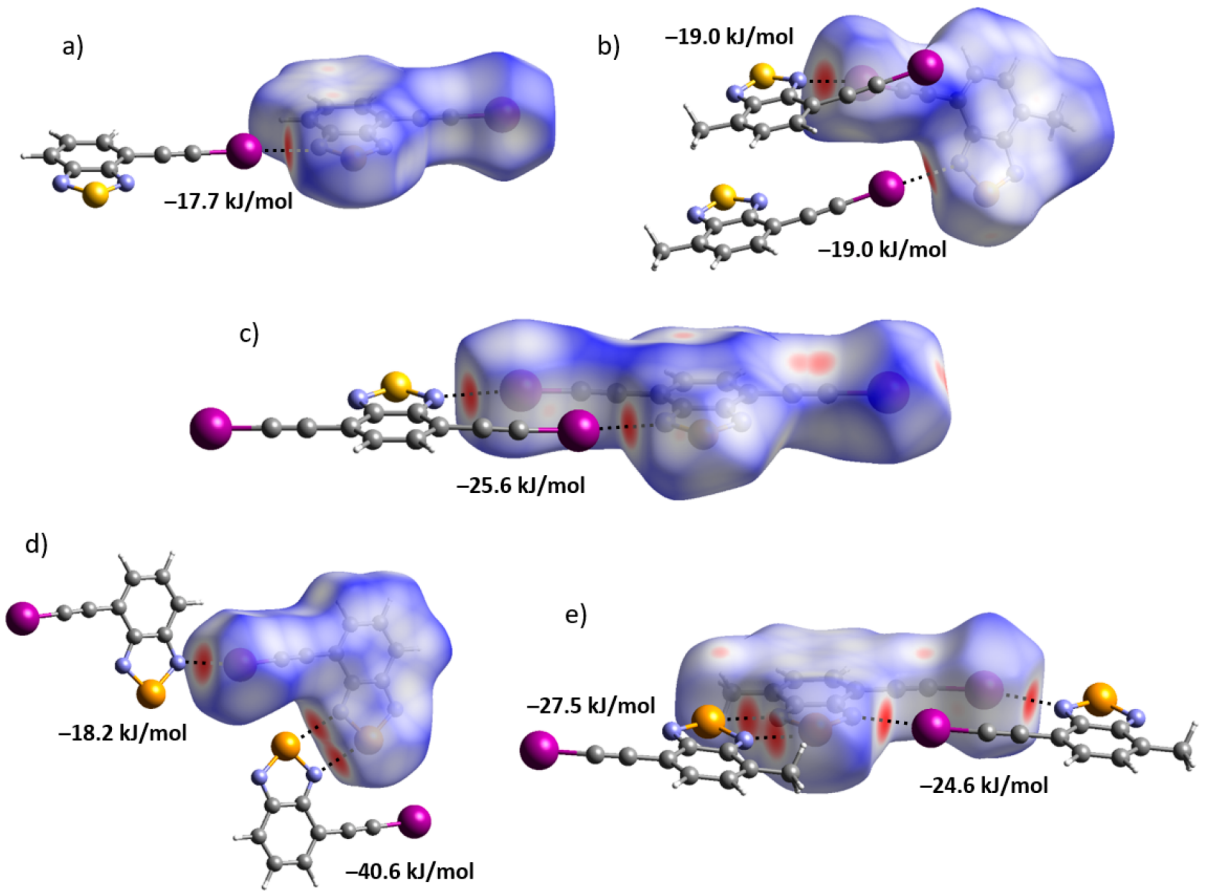

Figure 7. Hirshfeld surfaces of (a) [**S**]**CC-I**, (b) **CH$_3$**[**S**]**CC-I**, (c) [**S**](**CC-I**)$_2$, (d) [**Se**]**CC-I**, and (e) **CH$_3$**[**Se**]**CC-I** mapped with d_{norm}. Selected neighboring molecules forming close contacts are shown along with the values of calculated interaction energies between the molecules.

−19.0 kJ mol^{-1}, respectively (Figure 7a,b). In [**S**](**CC-I**)$_2$, apart from the N···I contacts, the intermolecular C≡C−I···π(ethynyl) contact (involving I2 and C9≡C10 atoms) are shown as a pale red area, thus suggesting a weak nature of this interaction. In this case, the strength of a single N···I bond is −12.8 kJ mol^{-1} and it is weaker in comparison to the remaining thiadiazoles (Figure 7c). In [**Se**]**CC-I** and **CH$_3$**[**Se**]-**CC-I**, the N···I and N···Se bonds displayed equally intense red spots. In the latter, there were two N···I (N1A···I1B and N1B···I1A) and two N···Se (Se1B···N2A and Se1A···N2B) interactions with slightly different parameters. The interaction energies of both XBs and ChBs in [**Se**]**CC-I** were lower than those in **CH$_3$**[**Se**]**CC-I** (Figure 7d,e).

In addition, we carried out an analysis of the specific types of intermolecular contacts found in the crystal networks with 2D fingerprint plots (Figure 8). The full plots showed a distribution pattern of all the interactions across the surface of a molecule, whereas decomposed plots provided the contribution of particular internal contacts observed in the crystal structures. The maps for the studied compounds clearly demonstrated the effect of the chalcogen as well as the substituent (H, CH$_3$, and iodoethynyl) at C7 on the packing of molecules. In particular, changes in contact distribution were observed for [**S**]**CC-I** and [**Se**]**CC-I**, which differ only in the chalcogen atom, and for [**Se**]**CC-I** and **CH$_3$**[**Se**]**CC-I**, which differ in the presence of the methyl substituent.

Among all the contacts between the atoms occurring on the Hirshfeld surfaces, intermolecular C···H and I···H interplay had the highest percentage for [**S**]**CC-I** (C···H 15.5% and I···H 20.1%), **CH$_3$**[**S**]**CC-I** (C···H 20.0% and I···H 19.7%), and **CH$_3$**[**Se**]**CC-I** (C···H 17.0% and I···H 20.9%)—almost 40% total in each case (Table S1 in the Supporting Information). This indicates that C···H and I···H contacts play an important role in the crystal packing of these molecules. For [**S**](**CC-I**)$_2$ C···H (14.1%) and N···I (13.8%) contacts and for [**Se**]**CC-I** C···H (17.0%) contacts have relatively high contribution in comparison to the other interactions in their crystal packing. The percentage distribution of all contacts based on fingerprint plots is shown in Table S1 in the Supporting Information.

It is worth pointing out that there is no correlation between the percentage contribution of specific contacts to the Hirshfeld surface and their strength. Taking into account the fact that supramolecular motifs are generally formed as a result of secondary bonding interactions, in analyzing the HS we particularly focused our attention on N···I contacts, which represent halogen interactions, and N···S or N···Se contacts, which represent ChBs (Figure 8). Both of them are directional and often play a significant structure-directing role in the self-assembly of molecules. From the plots we can see that the N···I contacts comprise no more than 14% of the total surface area for each compound and reach a maximum value of 13.8% for [**S**](**CC-I**)$_2$. It is important to note that in the crystal network of [**S**]**CC-I** out of the two possible N···I or N···S contacts only halogen interactions appear and comprise 7.5% of the whole surface. In all five compounds, the sum of the internal and external distances (d_i + d_e) for N···I is located at around 3.0 Å, which is less than the sum of the vdW radii of N (1.55 Å) and I (1.98 Å) atoms, indicating the strong nature of these contacts.

https://doi.org/10.1021/acs.cgd.1c01266
Cryst. Growth Des. 2022, 22, 1299−1311

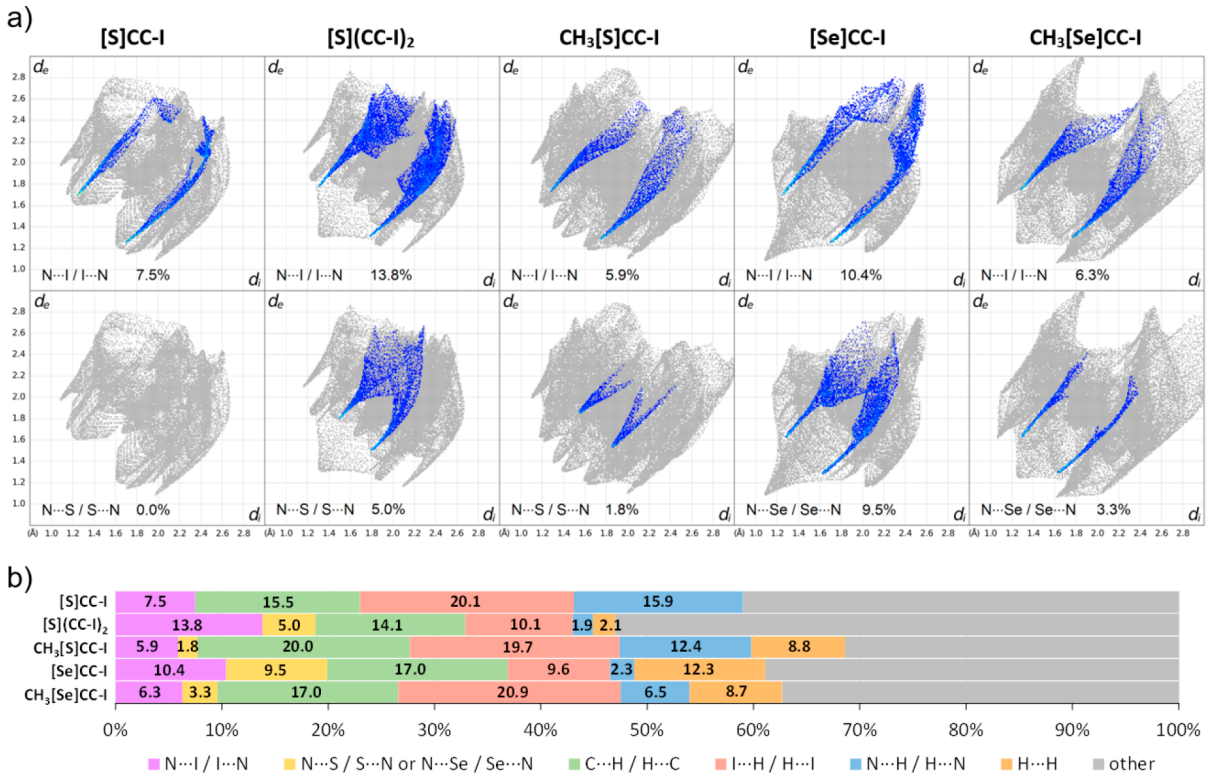

Figure 8. (a) Two-dimensional fingerprint plots decomposed into N···I/I···N (top) and N···S/S···N or N···Se/Se···N (bottom) contacts for all of the benzo-2,1,3-chalcogenadiazoles studied. The percentages of the contacts are presented at the bottom of each plot. The full fingerprint appears beneath each decomposed plot as a gray shadow. (b) Percentage contributions of selected close intermolecular contacts to the Hirshfeld surface area. Other contacts are highlighted in gray.

Table 5. Total Lattice Energies (E_{tot}) Obtained from CrystalExplorer and Theoretical Lattice Energies (E_L) Calculated with CRYSTAL09[a]

	CRYSTAL09			CrystalExplorer17
compound	E_c	E(D*)	$E_L = E_c + E(D^*) + E_{BSSE}$	E_{tot}
[S]CC-I	−17.4	−121.4	−97.3	−96.1
[Se]CC-I	−23.6	−132.8	−110.0	−109.7
[S](CC-I)$_2$	−1.1	−160.9	−103.7	−107.8
CH$_3$[S]CC-I	−6.6	−131.1	−93.0	−104.3
CH$_3$[Se]CC-I	−10.8	−148.7	−111.7	−99.8

[a]Contributions to the lattice energies: E_c (cohesive energy calculated from the difference in the electronic and nuclear repulsion energy of the bulk crystal and the molecules in the bulk), E(D*) (dispersive contribution derived from the modified Grimme model), and E_{BSSE} (basis set superposition error energy correction). The energies for a distance of 5 Å from the considered molecule in the crystal lattice are reported. All of the values are expressed in kJ mol^{-1}.

Furthermore, 2D fingerprint plots show potent N···Se interactions for both selenadiazole derivatives—the sum of d_i and d_e for N···Se is located at around 2.9 Å, which is also less than the sum of the vdW radii of N (1.55 Å) and Se (1.90 Å) atoms. Moreover, the long and needle-sharp peaks of the N···I halogen bond in **[S]CC-I** and N···Se ChB in **CH$_3$[Se]CC-I** indicate the directional nature of these interactions.

Lattice Energies and Energy Frameworks. The magnitude of the forces that hold the molecules in a crystal together is one of the most important thermodynamic parameters of a crystalline solid (having an effect on many of its physicochemical properties). Thus, we decided to investigate the overall interactions that contribute to the energy of a crystal lattice. The total lattice energies (E_L) for all five studied crystals were calculated using the CRYSTAL09 and CrystalExplorer17 programs, and the results are shown in Table 5. The values of E_L predicted by CRYSTAL09 for the thiadiazole derivatives are −93.0, −97.3, and −103.7 kJ mol^{-1} for **CH$_3$[S]CC-I**, **[S]CC-I**, and **[S](CC-I)$_2$**, respectively. The difference between the most and the least stable crystal lattice in this series is about 10 kJ mol^{-1}. From the results it can be concluded that the methyl substituent in **CH$_3$[S]CC-I** slightly decreases the crystal lattice stability in comparison to the iodoethynyl moiety in **[S](CC-I)$_2$**. For the selenadiazoles **CH$_3$[Se]CC-I** and **[Se](CC-I)$_2$**, the total lattice energies are lower and equal to about −110 kJ mol^{-1} regardless of the substituent (methyl or iodoethynyl) present in their structures. Moreover, the calculations clearly indicate a substantial contribution of the dispersive term E(D*) to the total lattice energies over the cohesive component E_c for all of the studied compounds. This means that the intermolecular C−H···π(ethynyl) and π···π interactions, regarded as the

https://doi.org/10.1021/acs.cgd.1c01266
Cryst. Growth Des. 2022, 22, 1299−1311

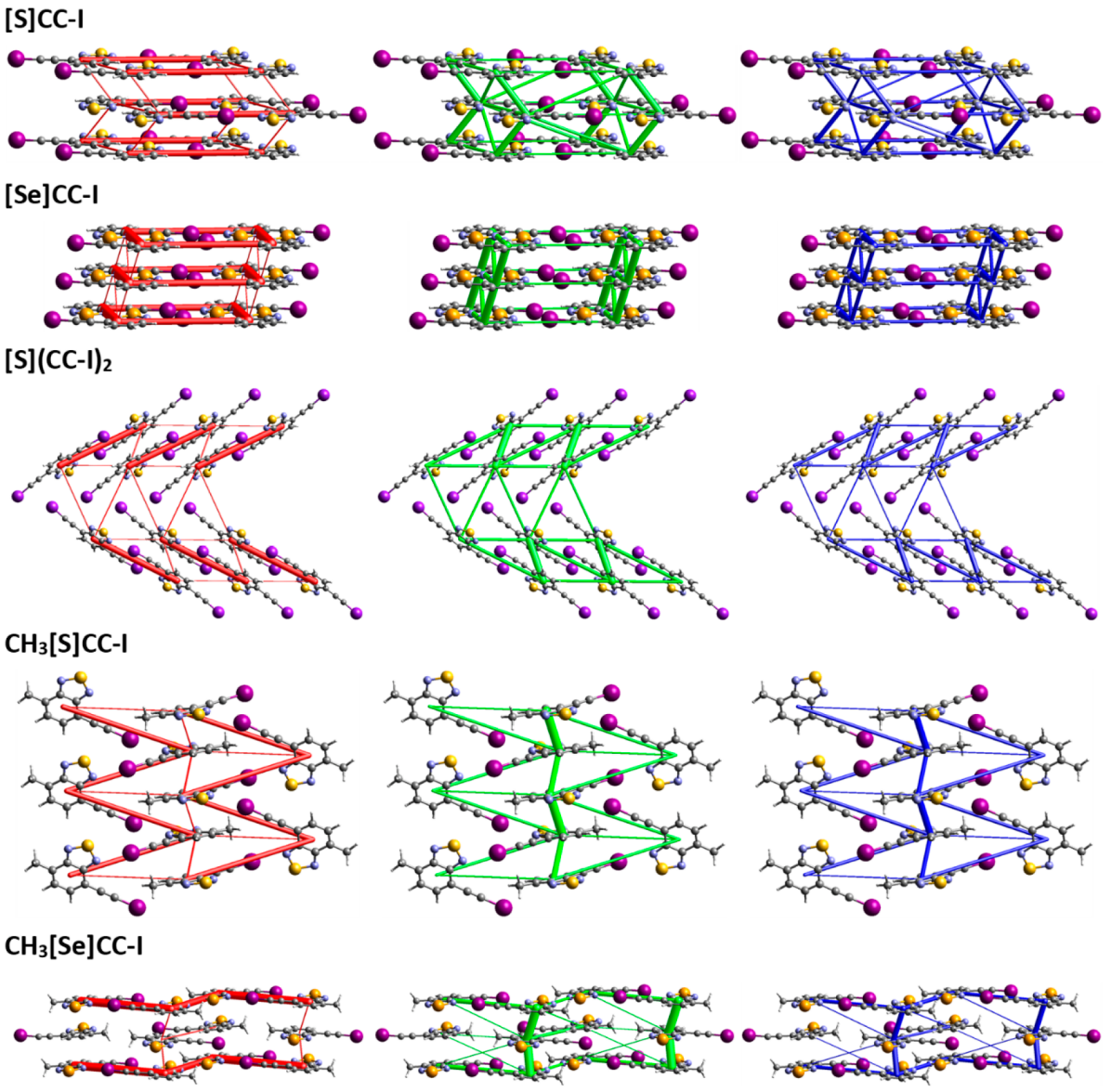

Figure 9. Energy frameworks for all benzo-2,1,3-chalcogenadiazole derivatives. Electrostatic (red), dispersion (green), and total (blue) interaction energies are shown as cylindrical tubes whose diameters are proportional to the magnitude of the energies. The tubes were adjusted to the same scale factor of 75 with a cutoff value of 5 kJ mol^{-1}.

$E(D^*)$ constituent, are crucial for the crystal lattice stability. The intermolecular ≡C−I···N XB and/or the Se···N ChBs, included mainly in E_c, have a much lower effect. They do not exceed 10% of the total lattice energy in the case of all 4,7-disubstituted benzo-2,1,3-chalcogenadiazoles (only 1% for [**S**](**CC-I**)$_2$). The Coulomb force (the major part of E_c) contributing to the total stabilization energy reached the highest value for [**S**]**CC-I** and [**Se**]**CC-I** (about 20%). Despite methodological differences resulting from the different wave functions implemented in both programs, the total lattice energies for studied compounds computed using CrystalExplorer17 correlate well with the results obtained from CRYSTAL09. The highest agreement in the magnitude of energy was obtained for [**S**]**CC-I** and [**Se**]**CC-I** (Table 5).

The contributions of the electrostatic (Coulombic) and dispersion components to the total energy within the studied crystals are visualized in the energy frameworks (Figure 9). The strongest electrostatic forces are depicted as wide cylindrical red tubes. In [**S**]**CC-I**, they are located between the adjacent molecules, which contact via ≡C−I···N bonds, generating infinite straight chains. The dispersion energy represented by the green bars forms a more complex structure. The larger bars are arranged in a zigzag pattern along the *b* axis connecting the neighboring layers. They mainly reflect the $\pi\cdots\pi$ stacking interactions of aromatic rings that are 3.545 Å apart (Table 2).

The topology of the electrostatic energy frameworks for [**Se**]**CC-I** is a parallelogram formed by two intermolecular Se···N ChBs (stronger, wider cylinders) and two ≡C−I···N XBs (weaker, thinner tubes), which are slightly shifted in the same direction between the neighboring layers. The dispersion energy framework shows that the most robust interactions are located between the overlapping aromatic rings of the molecules in the adjacent layers spreading along the *a* axis. Larger red tubes in the crystal lattice of [**S**](**CC-I**)$_2$ are visible in the dimers. They correspond to two ≡C−I···N XBs stabilizing the $R_2^2(12)$ supramolecular motif. Smaller tubes present in the single layer as well as between them form a

https://doi.org/10.1021/acs.cgd.1c01266
Cryst. Growth Des. 2022, 22, 1299−1311

fused-triangle topology, which represents the ≡C−I···π XB. In the dispersion energy, frameworks with the strongest interactions are visible between the aromatic rings of the adjacent dimers and they form a zigzag pattern along the *a* axis. In **CH_3[S]CC-I**, the dispersion component forms zigzag chains in which cylindrical green tubes connect the aromatic rings of the molecules belonging to two interpenetrating helices. The Coulombic forces also generate a zigzag that runs along the helix axis. They reflect the ≡C−I···N interactions between the adjacent molecules within the helix. The energy frameworks for the crystal structure of **CH_3[Se]CC-I** are entirely different from those for **CH_3[S]CC-I**. In **CH_3[Se]CC-I**, both energy components show a zigzag topology but are arranged in various directions; the electrostatic component being horizontal (along with the layers and the *c* axis) and the dispersion component being vertical (across the layers, along the *a* axis).

CONCLUSIONS

In summary, we presented the results of experimental crystallographic studies in conjunction with quantum-chemical calculations for a series of novel iodoethynyl-substituted benzo-2,1,3-chalcogenadiazoles, which have the potential to aggregate during the crystallization process through either halogen- or chalcogen-bonding interactions or both. Considering the obtained results, we came to the conclusion that the chalcogen atom in these compounds is a primary factor determining the type of the observed interactions and consequently is responsible for the organization of the molecules in the solid state. In the thiadiazoles studied, the ≡C−I···N halogen bonds are the leading directional interactions that determine the emergence of specific motifs in the crystal: chains, dimers, and helices for **[S]CC-I**, **[S](CC-I)$_2$** and **CH_3[S]CC-I**, respectively. However, in the case of the bis(iodoethynyl) derivative the ≡C−I···π(ethynyl) halogen bonding additionally contributes to the self-assembly of the crystal. Furthermore, in the crystal networks of the analogous selenadiazoles, apart from the ≡C−I···N halogen interactions, self-complementary $[Se\cdots N]_2$ chalcogen interactions were also observed. The cooperation of these forces organizes the molecules into an array of chalcogen-bonded dimers forming polymeric chain structures with the use of halogen bonds. Their architecture depends on the different σ-holes on the selenium atom used for the formation of the $[Se\cdots N]_2$ synthon.

The calculated total lattice energies indicate that, although the cooperativity of halogen and chalcogen bonds determine short-range supramolecular order, the contribution of the aromatic $\pi\cdots\pi$ interactions is also an important factor that determines the molecular packing of the crystals. For all of the studied compounds, the dispersive components make a higher contribution to the total lattice energies in comparison to the cohesive terms. Furthermore, an analysis of the fingerprint plots showed that the changes in the intercontact distribution observed in the crystal structures depend on the substituent (H, CH_3, or iodoethynyl) in the benzene ring of the title benzo-2,1,3-chalcogenadiazoles.

ASSOCIATED CONTENT

Supporting Information

The Supporting Information is available free of charge at https://pubs.acs.org/doi/10.1021/acs.cgd.1c01266.

Details of the synthetic procedures, NMR spectra, ORTEP representations, PXRD patterns, and percentage contributions of all contacts to the Hirshfeld surfaces (PDF)

Accession Codes

CCDC 2101344−2101348 contain the supplementary crystallographic data for this paper. These data can be obtained free of charge via www.ccdc.cam.ac.uk/data_request/cif, or by emailing data_request@ccdc.cam.ac.uk, or by contacting The Cambridge Crystallographic Data Centre, 12 Union Road, Cambridge CB2 1EZ, UK; fax: +44 1223 336033.

AUTHOR INFORMATION

Corresponding Author

Teresa Olszewska − *Department of Organic Chemistry, Faculty of Chemistry, Gdańsk University of Technology, 80-233 Gdańsk, Poland;* orcid.org/0000-0003-1477-1562; Phone: +48 58 347 14 25; Email: teresa.olszewska@pg.edu.pl

Authors

Jan Alfuth − *Department of Organic Chemistry, Faculty of Chemistry, Gdańsk University of Technology, 80-233 Gdańsk, Poland*

Beata Zadykowicz − *Luminescence Research Group, Faculty of Chemistry, University of Gdańsk, 80-308 Gdańsk, Poland;* orcid.org/0000-0002-7125-5233

Barbara Wicher − *Department of Chemical Technology of Drugs, Poznań University of Medical Sciences, 60-780 Poznań, Poland;* orcid.org/0000-0003-2254-2508

Katarzyna Kazimierczuk − *Department of Inorganic Chemistry, Faculty of Chemistry, Gdańsk University of Technology, 80-233 Gdańsk, Poland*

Tadeusz Połoński − *Department of Organic Chemistry, Faculty of Chemistry, Gdańsk University of Technology, 80-233 Gdańsk, Poland*

Complete contact information is available at: https://pubs.acs.org/10.1021/acs.cgd.1c01266

Author Contributions

The manuscript was written through contributions of all authors. All authors have given approval to the final version of the manuscript.

Notes

The authors declare no competing financial interest.

ACKNOWLEDGMENTS

We thank the Wroclaw Centre for Networking and Supercomputing (WCSS) for the possibility of conducting calculations on its computers (Grant No. 215). The work benefited from the facilities of the Poznan University Medical Sciences Core Facility.

REFERENCES

(1) Desiraju, G. R. Crystal Engineering: A Holistic View. *Angew. Chemie Int. Ed.* **2007**, *46*, 8342−8356.

(2) Desiraju, G. R. Crystal Engineering: A Brief Overview. *J. Chem. Sci.* **2010**, *122*, 667−675.

(3) Scheiner, S. Understanding Noncovalent Bonds and Their Controlling Forces. *J. Chem. Phys.* **2020**, *153*, 140901.

(4) Thakuria, R.; Nath, N. K.; Saha, B. K. The Nature and Applications of π-π Interactions: A Perspective. *Cryst. Growth Des.* **2019**, *19*, 523−528.

(5) Gilli, G.; Gilli, P. *The Nature of the Hydrogen Bond*; Oxford University Press: 2009.

(6) Bauzá, A.; Mooibroek, T. J.; Frontera, A. The Bright Future of Unconventional σ/π-Hole Interactions. *ChemPhysChem* **2015**, *16*, 2496−2517.
(7) Kolář, M. H.; Hobza, P. Computer Modeling of Halogen Bonds and Other σ-Hole Interactions. *Chem. Rev.* **2016**, *116*, 5155−5187.
(8) Brammer, L. Halogen Bonding, Chalcogen Bonding, Pnictogen Bonding, Tetrel Bonding: Origins, Current Status and Discussion. *Faraday Discuss.* **2017**, *203*, 485−507.
(9) Scheiner, S. Detailed Comparison of the Pnicogen Bond with Chalcogen, Halogen, and Hydrogen Bonds. *Int. J. Quantum Chem.* **2013**, *113*, 1609−1620.
(10) Mahmudov, K. T.; Gurbanov, A. V.; Aliyeva, V. A.; Resnati, G.; Pombeiro, A. J. L. Pnictogen Bonding in Coordination Chemistry. *Coord. Chem. Rev.* **2020**, *418*, 213381.
(11) Mahmudov, K. T.; Kopylovich, M. N.; Guedes Da Silva, M. F. C.; Pombeiro, A. J. L. Chalcogen Bonding in Synthesis, Catalysis and Design of Materials. *Dalton Trans.* **2017**, *46*, 10121−10138.
(12) Vogel, L.; Wonner, P.; Huber, S. M. Chalcogen Bonding: An Overview. *Angew. Chemie Int. Ed.* **2019**, *58*, 1880−1891.
(13) Cavallo, G.; Metrangolo, P.; Milani, R.; Pilati, T.; Priimagi, A.; Resnati, G.; Terraneo, G. The Halogen Bond. *Chem. Rev.* **2016**, *116*, 2478−2601.
(14) Gilday, L. C.; Robinson, S. W.; Barendt, T. A.; Langton, M. J.; Mullaney, B. R.; Beer, P. D. Halogen Bonding in Supramolecular Chemistry. *Chem. Rev.* **2015**, *115*, 7118−7195.
(15) Desiraju, G. R.; Shing Ho, P.; Kloo, L.; Legon, A. C.; Marquardt, R.; Metrangolo, P.; Politzer, P.; Resnati, G.; Rissanen, K. Definition of the Halogen Bond (IUPAC Recommendations 2013). *Pure Appl. Chem.* **2013**, *85*, 1711−1713.
(16) De Vleeschouwer, F.; Denayer, M.; Pinter, B.; Geerlings, P.; De Proft, F. Characterization of Chalcogen Bonding Interactions via an In-Depth Conceptual Quantum Chemical Analysis. *J. Comput. Chem.* **2018**, *39*, 557−572.
(17) Braga, D.; Desiraju, G. R.; Miller, J. S.; Orpen, A. G.; Price, S. L. Innovation in Crystal Engineering. *CrystEngComm* **2002**, *4*, 500−509.
(18) Whitesides, G. M.; Grzybowski, B. Self-Assembly at All Scales. *Science* **2002**, *295*, 2418−2421.
(19) Tiekink, E. R.; Vittal, J. *Frontiers in Crystal Engineering*; Wiley: 2006.
(20) Aakeröy, C. B.; Bryce, D. L.; Desiraju, G. R.; Frontera, A.; Legon, A. C.; Nicotra, F.; Rissanen, K.; Scheiner, S.; Terraneo, G.; Metrangolo, P.; Resnati, G. Definition of the Chalcogen Bond (IUPAC Recommendations 2019). *Pure Appl. Chem.* **2019**, *91*, 1889−1892.
(21) Gleiter, R.; Haberhauer, G.; Werz, D. B.; Rominger, F.; Bleiholder, C. From Noncovalent Chalcogen-Chalcogen Interactions to Supramolecular Aggregates: Experiments and Calculations. *Chem. Rev.* **2018**, *118*, 2010−2041.
(22) Ho, P. C.; Szydlowski, P.; Sinclair, J.; Elder, P. J. W.; Kübel, J.; Gendy, C.; Lee, L. M.; Jenkins, H.; Britten, J. F.; Morim, D. R.; Vargas-Baca, I. Supramolecular Macrocycles Reversibly Assembled by Te···O Chalcogen Bonding. *Nat. Commun.* **2016**, *7*, 11299.
(23) Zeng, R.; Gong, Z.; Yan, Q. Chalcogen-Bonding Supramolecular Polymers. *J. Org. Chem.* **2020**, *85*, 8397−8404.
(24) Xiao, Y.-L.; Zhang, B.; He, C.-Y.; Zhang, X. Direct Olefination of Fluorinated Benzothiadiazoles: A New Entry to Optoelectronic Materials. *Chem. Eur. J.* **2014**, *20*, 4532−4536.
(25) Flood, A.; Trujillo, C.; Sanchez-Sanz, G.; Kelly, B.; Muguruza, C.; Callado, L. F.; Rozas, I. Thiophene/Thiazole-Benzene Replacement on Guanidine Derivatives Targeting α2-Adrenoceptors. *Eur. J. Med. Chem.* **2017**, *138*, 38−50.
(26) Biot, N.; Bonifazi, D. Chalcogen-Bond Driven Molecular Recognition at Work. Coord. *Chem. Rev.* **2020**, *413*, 213243.
(27) Benz, S.; López-Andarias, J.; Mareda, J.; Sakai, N.; Matile, S. Catalysis with Chalcogen Bonds. *Angew. Chem.* **2017**, *129*, 830−833.
(28) Benz, S.; Poblador-Bahamonde, A. I.; Low-Ders, N.; Matile, S. Catalysis with Pnictogen, Chalcogen, and Halogen Bonds. *Angew. Chemie Int. Ed.* **2018**, *57*, 5408−5412.
(29) Wonner, P.; Vogel, L.; Düser, M.; Gomes, L.; Kniep, F.; Mallick, B.; Werz, D. B.; Huber, S. M. Carbon-Halogen Bond Activation by Selenium-Based Chalcogen Bonding. *Angew. Chemie Int. Ed.* **2017**, *56*, 12009−12012.
(30) Wonner, P.; Vogel, L.; Kniep, F.; Huber, S. M. Catalytic Carbon-Chlorine Bond Activation by Selenium-Based Chalcogen Bond Donors. *Chem. Eur. J.* **2017**, *23*, 16972−16975.
(31) Wang, H.; Wang, W.; Jin, W. J. σ-Hole Bond vs π-Hole Bond: A Comparison Based on Halogen Bond. *Chem. Rev.* **2016**, *116*, 5072−5104.
(32) Scilabra, P.; Terraneo, G.; Resnati, G. The Chalcogen Bond in Crystalline Solids: A World Parallel to Halogen Bond. *Acc. Chem. Res.* **2019**, *52*, 1313−1324.
(33) Brezgunova, M. E.; Lieffrig, J.; Aubert, E.; Dahaoui, S.; Fertey, P.; Lebègue, S.; Angyán, J. G.; Fourmigué, M.; Espinosa, E. Chalcogen Bonding: Experimental and Theoretical Determinations from Electron Density Analysis. Geometrical Preferences Driven by Electrophilic-Nucleophilic Interactions. *Cryst. Growth Des.* **2013**, *13*, 3283−3289.
(34) Bertini, V.; Dapporto, P.; Lucchesini, F.; Sega, A.; De Munno, A. 1,2,5-Telluradiazole, $C_2H_2N_2Te$. *Acta Crystallogr. Sect. C* **1984**, *40*, 653−655.
(35) Cozzolino, A. F.; Yang, Q.; Vargas-Baca, I. Engineering Second-Order Nonlinear Optical Activity by Means of a Noncentrosymmetric Distortion of the $[Te\text{-}N]_2$ Supramolecular Synthon. *Cryst. Growth Des.* **2010**, *10*, 4959−4964.
(36) Neidlein, R.; Knecht, D.; Gieren, A.; Ruiz-Pérez, C. Synthese Und Röntgenstrukturanalyse Des Phenanthro[9,10-*c*]-1,2,5-Telluradiazols. *Zeitschrift für Naturforsch.* **1987**, *42*, 84−90.
(37) Xu, Y.; Kumar, V.; Bradshaw, M. J. Z.; Bryce, D. L. Chalcogen-Bonded Cocrystals of Substituted Pyridine *N*-Oxides and Chalcogenodiazoles: An X-Ray Diffraction and Solid-State NMR Investigation. *Cryst. Growth Des.* **2020**, *20*, 7910−7920.
(38) Kumar, V.; Xu, Y.; Bryce, D. L. Double Chalcogen Bonds: Crystal Engineering Stratagems via Diffraction and Multinuclear Solid-State Magnetic Resonance Spectroscopy. *Chem. Eur. J.* **2020**, *26*, 3275−3286.
(39) Cozzolino, A. F.; Britten, J. F.; Vargas-Baca, I. The Effect of Steric Hindrance on the Association of Telluradiazoles through Te-N Secondary Bonding Interactions. *Cryst. Growth Des.* **2006**, *6*, 181−186.
(40) Biot, N.; Bonifazi, D. Programming Recognition Arrays through Double Chalcogen-Bonding Interactions. *Chem. Eur. J.* **2018**, *24*, 5439−5443.
(41) Lee, L. M.; Corless, V.; Luu, H.; He, A.; Jenkins, H.; Britten, J. F.; Adam Pani, F.; Vargas-Baca, I. Synthetic and Structural Investigations of Bis(*N*-Alkyl-Benzoselenadiazolium) Cations. *Dalton Trans.* **2019**, *48*, 12541−12548.
(42) Biot, N.; Romito, D.; Bonifazi, D. Substituent-Controlled Tailoring of Chalcogen-Bonded Supramolecular Nanoribbons in the Solid State. *Cryst. Growth Des.* **2021**, *21*, 536−543.
(43) Lee, L. M.; Corless, V. B.; Tran, M.; Jenkins, H.; Britten, J. F.; Vargas-Baca, I. Synthetic, Structural, and Computational Investigations of *N*-Alkyl Benzo-2,1,3-Selenadiazolium Iodides and Their Supramolecular Aggregates. *Dalton Trans.* **2016**, *45*, 3285−3293.
(44) Alfuth, J.; Zadykowicz, B.; Sikorski, A.; Połoński, T.; Eichstaedt, K.; Olszewska, T. Effect of Aromatic System Expansion on Crystal Structures of 1,2,5-Thia- and 1,2,5-Selenadiazoles and Their Quaternary Salts: Synthesis, Structure, and Spectroscopic Properties. *Materials* **2020**, *13*, 4908.
(45) Eichstaedt, K.; Wasilewska, A.; Wicher, B.; Gdaniec, M.; Połoński, T. Supramolecular Synthesis Based on a Combination of Se···N Secondary Bonding Interactions with Hydrogen and Halogen Bonds. *Cryst. Growth Des.* **2016**, *16*, 1282−1293.
(46) Biot, N.; Bonifazi, D. Concurring Chalcogen- and Halogen-Bonding Interactions in Supramolecular Polymers for Crystal Engineering Applications. *Chem. Eur. J.* **2020**, *26*, 2904−2913.
(47) Panikkattu, V. V.; Tran, A.; Sinha, A. S.; Reinheimer, E. W.; Guidez, E. B.; Aakeröy, C. B. Traversing the Tightrope between

https://doi.org/10.1021/acs.cgd.1c01266
Cryst. Growth Des. 2022, 22, 1299−1311

Halogen and Chalcogen Bonds Using Structural Chemistry and Theory. *Cryst. Growth Des.* **2021**, *21*, 7168−7178.
(48) Fourmigué, M. Halogen Bonding: Recent Advances. *Curr. Opin. Solid State Mater. Sci.* **2009**, *13*, 36−45.
(49) Spackman, M. A.; Jayatilaka, D. Hirshfeld Surface Analysis. *CrystEngComm* **2009**, *11*, 19−32.
(50) Tan, S. L.; Jotani, M. M.; Tiekink, E. R. T. Utilizing Hirshfeld Surface Calculations, Non-Covalent Interaction (NCI) Plots and the Calculation of Interaction Energies in the Analysis of Molecular Packing. *Acta Crystallogr. Sect. E* **2019**, *75*, 308−318.
(51) *CrysAlisPro Software System, Ver. 171.41*; Rigaku Corporation: 2020.
(52) Clark, R. C.; Reid, J. S. The Analytical Calculation of Absorption in Multifaceted Crystals. *Acta Crystallogr., Sect. A* **1995**, *51*, 887−897.
(53) Sheldrick, G. M. SHELXT - Integrated Space-Group and Crystal-Structure Determination. *Acta Crystallogr., Sect. A* **2015**, *71*, 3−8.
(54) Dolomanov, O. V.; Bourhis, L. J.; Gildea, R. J.; Howard, J. A. K.; Puschmann, H. OLEX2: A Complete Structure Solution, Refinement and Analysis Program. *J. Appl. Crystallogr.* **2009**, *42*, 339−341.
(55) Frisch, M. J.; Trucks, G. W.; Schlegel, H. B.; Scuseria, G. E.; Robb, M. A.; Cheeseman, J. R.; Scalmani, G.; Barone, V.; Mennucci, B.; Petersson, G. A.; Nakatsuji, H.; Caricato, M.; Li, X.; Hratchian, H. P.; Izmaylov, A. F.; Bloino, J.; Zheng, G.; Sonnenberg, J. L.; Hada, M.; Ehara, M.; Toyota, K.; Fukuda, R.; Hasegawa, J.; Ishida, M.; Nakajima, T.; Honda, Y.; Kitao, O.; Nakai, H.; Vreven, T.; Montgomery, J. A., Jr.; Peralta, J. E.; Ogliaro, F.; Bearpark, M. J.; Heyd, J. J.; Brothers, E. N.; Kudin, K. N.; Staroverov, V. N.; Kobayashi, R.; Normand, J.; Raghavachari, K.; Rendell, A. P.; Burant, J. C.; Iyengar, S. S.; Tomasi, J.; Cossi, M.; Rega, N.; Millam, J. M.; Klene, M.; Knox, J. E.; Cross, J. B.; Bakken, V.; Adamo, C.; Jaramillo, J.; Gomperts, R.; Stratmann, R. E.; Yazyev, O.; Austin, A. J.; Cammi, R.; Pomelli, C.; Ochterski, J. W.; Martin, J. R.; Morokuma, K.; Zakrzewski, V. G.; Voth, G. A.; Salvador, P.; Dannenberg, J. J.; Dapprich, S.; Daniels, D. A.; Farkas, O.; Foresman, J. B.; Ortiz, J. V.; Cioslowski, J.; Fox, D. J. *Gaussian 09 (Rev. A.02)*; Gaussian, Inc.: 2009.
(56) Labanowski, J. K.; Andzelm, J. K. *Density Functional Methods in Chemistry*; Springer: 1991.
(57) Becke, A. D. Density-Functional Exchange-Energy Approximation with Correct Asymptotic Behavior. *Phys. Rev. A* **1988**, *38*, 3098−3100.
(58) Becke, A. D. Density-Functional Thermochemistry. III. The Role of Exact Exchange. *J. Chem. Phys.* **1993**, *98*, 5648−5652.
(59) Hehre, W. J. Ab Initio Molecular Orbital Theory. *Acc. Chem. Res.* **1976**, *9*, 399−406.
(60) Hariharan, P. C.; Pople, J. A. The Influence of Polarization Functions on Molecular Orbital Hydrogenation Energies. *Theor. Chim. Acta* **1973**, *28*, 213−222.
(61) Dobbs, K. D.; Hehre, W. J. Molecular Orbital Theory of the Properties of Inorganic and Organometallic Compounds 4. Extended Basis Sets for Third-and Fourth-row, Main-group Elements. *J. Comput. Chem.* **1986**, *7*, 359−378.
(62) Mahmoudi, G.; Castiñeiras, A.; Garczarek, P.; Bauzá, A.; Rheingold, A. L.; Kinzhybalo, V.; Frontera, A. Synthesis, X-Ray Characterization, DFT Calculations and Hirshfeld Surface Analysis of Thiosemicarbazone Complexes of Mn^{+} Ions (n = 2, 3; M = Ni, Cd, Mn, Co and Cu). *CrystEngComm* **2016**, *18*, 1009−1023.
(63) Abeysekera, A. M.; Day, V. W.; Sinha, A. S.; Aakeröy, C. B. Mapping out the Relative Influence of Hydrogen and Halogen Bonds in Crystal Structures of a Family of Amide-Substituted Pyridines. *Cryst. Growth Des.* **2020**, *20*, 7399−7410.
(64) De Silva, V.; Averkiev, B. B.; Sinha, A. S.; Aakeröy, C. B. The Balance between Hydrogen Bonds, Halogen Bonds, and Chalcogen Bonds in the Crystal Structures of a Series of 1,3,4-Chalcogenadiazoles. *Molecules* **2021**, *26*, 4125.
(65) Dennington, R. D.; Keith, T. A.; Millam, J. M. *GaussView, Ver. 5.0.8*; Semichem Inc.: 2008.
(66) Dovesi, R.; Sauders, V. R.; Roetti, C.; Orlando, R.; Zicovich-Wilson, C. M.; Pascale, F.; Civalleri, B.; Doll, K.; Harrison, N. M.; Bush, I. J.; D'Arco, P.; Llunell, M. *Crystal09*; Universita di Torino: 2009.
(67) Civalleri, B.; Zicovich-Wilson, C. M.; Valenzano, L.; Ugliengo, P. B3LYP Augmented with an Empirical Dispersion Term (B3LYP-D*) as Applied to Molecular Crystals. *CrystEngComm* **2008**, *10*, 405−410.
(68) Grimme, S. Semiempirical GGA-Type Density Functional Constructed with a Long-Range Dispersion Correction. *J. Comput. Chem.* **2006**, *27*, 1787−1799.
(69) Grimme, S. Accurate Description of van Der Waals Complexes by Density Functional Theory Including Empirical Corrections. *J. Comput. Chem.* **2004**, *25*, 1463−1473.
(70) Boys, S. F.; Bernardi, F. The Calculation of Small Molecular Interactions by the Differences of Separate Total Energies. Some Procedures with Reduced Errors. *Mol. Phys.* **1970**, *19*, 553−566.
(71) Turner, M. J.; McKinnon, J. J.; Wolff, S. K.; Grimwood, D. J.; Spackman, P. R.; Jayatilaka, D.; Spackman, M. A. *CrystalExplorer17*; University of Western Australia: 2017.
(72) Roothaan, C. C. J. New Developments in Molecular Orbital Theory. *Rev. Mod. Phys.* **1951**, *23*, 69−89.
(73) Binkley, J. S.; Pople, J. A.; Hehre, W. J. Self-Consistent Molecular Orbital Methods. 21. Small Split-Valence Basis Sets for First-Row Elements. *J. Am. Chem. Soc.* **1980**, *102*, 939−947.
(74) Garrett, G. E.; Gibson, G. L.; Straus, R. N.; Seferos, D. S.; Taylor, M. S. Chalcogen Bonding in Solution: Interactions of Benzotelluradiazoles with Anionic and Uncharged Lewis Bases. *J. Am. Chem. Soc.* **2015**, *137*, 4126−4133.

https://doi.org/10.1021/acs.cgd.1c01266
Cryst. Growth Des. 2022, 22, 1299−1311